FMT-2 Discharge Cathode Erosion Rate Measurements via Laser-Induced Fluorescence

G. J. Williams, Jr., T. B. Smith, K. H. Glick, Y. Hidaka,[***] and
A. D. Gallimore[****]

Relative erosion-rates and impingement ion production mechanisms have been identified for the discharge cathode of a 30 cm ion engine using laser-induced fluorescence (LIF). Mo and W erosion products as well as neutral and singly ionized xenon were interrogated. The erosion increases with both discharge current and voltage and spatially resolved measurements agree with observed erosion patterns. Ion velocity mapping identified back-flowing ions near the regions of erosion with energies sufficient to generate the level of observed erosion. A potential-hill downstream of the cathode was indicated and is suggested to be responsible for the erosion.

Nomenclature

A_{ij} Einstein A coefficient (s^{-1})
c   Speed of light ($2.998 \cdot 10^8$ m/s)
E_{ij} Transition energy (eV)
e   Electron charge ($1.602 \cdot 10^{-19}$ C)
h   Plank's Constant ($6.626 \cdot 10^{-34}$ Js)
f   Oscillator strength
g_i Degeneracy of state i
g( )Gaussian line shape (s)
G   Gaunt factor
I   Intensity ($W/m^{2)}$
I_{SAT} Saturation Intensity (W/m^2)
k   Boltzman constant ($1.381 \cdot 10^{-23}$ J/K)
l( ) Power broadened line shape (s)
m   Mass (kg)
n   Number density (m^{-3})
R_{CD} Collisional depopulation rate ($m^3 \ s^{-1}$)
T   Temperature (K)
v   Velocity (m/s)

     Homogeneous relaxation rate (Hz)
     Wavelength (m)
     Frequency (Hz)
     Cross-section (m^2)

Introduction

Ion thrusters are being scaled to different powers and operating conditions for space flight applications. A baseline for this scaling is the NASA Solar Electric Propulsion Technology Readiness (NSTAR) 30 cm ion thruster. Several wear-tests have been conducted to demonstrate long duration operation and life-limiting phenomena. One of the potential failure mechanisms identified during these tests was erosion of the discharge cathode assembly.

Severe erosion of the outer edge of the orifice plate, W at 145 µm/khr; of the tip of the cathode tube, Mo at 280 µm/khr; and of the heater coil outer sheath, Ta, were observed in the 2000 hr development wear-test.[1] The erosion pattern is highlighted in Fig. 1a. A keeper electrode was introduced as an engineering solution, and, after subsequent 1000 hr and 8200 hr wear-tests the observed erosion was reduced to less than 3 µm/khr.[2,3] Shown in a photo in Fig. 1b, this rate is significantly below the estimated acceptable threshold of 64 µm/khr based on the thickness of the keeper and on the location of the electron beam weld between the cathode tube and the orifice plate. It has been suggested that higher powers and longer periods of operation can be accommodated by thickening the orifice plates.[4] However, recent developments in cathode

assembly design may not make this a feasible option.[5,6]

The source of the high-energy ions causing the erosion has remained largely unknown. Ray-tracing after the 2000 hr test indicated the source of the ions was located between 1 and 11 mm downstream of the orifice plate. The potential-hill phenomenon, which has been postulated as the source of high-energy ions eroding downstream cathode-potential surfaces, is the leading explanation.[7] However, sheath effects may account for the erosion pattern and plasma oscillations might also yield the high-energy ions required for the erosion. Recent investigations have shown back-flowing ions near the face of the discharge cathode with concentrations sufficient to cause the observed erosion.[8]

Laser-induced fluorescence (LIF) was employed in this investigation to measure Xe II velocity distributions and Xe I, W and Mo concentrations near the exit of the discharge cathode. These investigations were conducted at the Plasmadynamics and Electric Propulsion Laboratory (PEPL) at the University of Michigan.

Apparatus and Procedure

Thruster

The functional model thrusters (FMTs) were the immediate predecessor to the NSTAR engineering model thrusters (EMTs) which preceded the NSTAR flight thrusters. The FMTs differed principally from the EMTs in their soft aluminum construction. The magnetic field, discharge cathode assembly (DCA), and geometry of the discharge chamber were identical to EMT-1's. The quartz windows replaced roughly twenty percent of the anode surface as shown in Fig. 2 and have had a negligible impact on discharge chamber and thruster performance. The thruster has been operated over the entire NSTAR power throttling range at both GRC and at PEPL using a SKIT-Pac provided by NASA GRC. Performance of the thruster is comparable to the engineering and flight model thrusters

The DCA was the same as that used during the second segment of the 2000 hr wear test. Measurements were made with and without the presence of a keeper electrode. Thruster operating conditions are summarized in Table 1 and correspond to points in the NSTAR throttling matrix.[9] Detailed dimensions of the components of the DCA are not provided as per an agreement with NASA GRC.

Vacuum Facility

This investigation was performed in the 6 m x 9 m large vacuum test facility (LVTF) at PEPL. Four CVI Model TM-1200 Re-Entrant Cryopumps provided a combined pumping speed of 140,000 l/s on xenon with a base pressure of less than $2\ 10^{-7}$ Torr. The back pressure during 2.3 kW operation was roughly $3\ 10^{-6}$ Torr, corrected for xenon.

Xenon flow was controlled to the thruster using a dedicated propellant feed system provided by NASA GRC. The flow rates were periodically calibrated using a bubble flow meter between tests. No significant variation was observed.

The FMT was mounted on a two-axis positioning system. Resolution was on the order of 0.025 cm for both stages. A 1.8 m by 2.5 m louvered graphite panel-beam dump protected windows downstream of the thruster and suppressed back sputtering. The panels were located roughly 4 m downstream of the thruster.

Laser and Optics

An argon-ion pumped dye laser (Coherent model 899-29 model) was used in single and in multiple-beam techniques.[10] Four-beam LIF (shown schematically in Fig. 3) measured three velocity components simultaneously: a second axial beam was used in the four-beam technique to increase the resolution of the axial velocity. Angles associated with the measurement of various components are given in Table 2. Both single and 4-beam techniques used a Hamamatsu reference cell to provide a zero velocity datum. The laser was typically scanned over a 0.01 nm interval in 0.061 pm increments. The beams were delivered to the thruster in a manner identical to that used in previous Hall thruster interrogations.[10] Alignment was facilitated by a wire crosshair on the side of the FMT plasma screen.

Wavelengths, transitions, energy levels, and saturation intensities associated with the interrogation of the various species are given in Table 3.[11,12] A sputtering target source incorporating a hollow cathode assembly (HCA) and a biased metallic target was used to verify the W and Mo species interrogation and optimal transition wavelengths. To facilitate data acquisition and signal comparison, the HCA and target were placed in the HVTF behind and on the centerline of the FMT. The sputtering source and the FMT were operated simultaneously.

Data were collected using Spex 500 M and Spex H10 monochromators fitted with Hamamatsu 928 PMT's. Both fluorescence signals were controlled and recorded via computers. The Spex 500 M monochromator's slits were set to 50 μm. Because of a 2x magnification, the effective spot size at the focus of the collection lens was 25 μm. The bi-conical sample volume in the cathode plume was roughly 0.5 cm long and 0.1 cm in diameter at its ends. Measurements taken far downstream of the cathode at low power indicate that the ambient plasma outside of the cathode plume contributes less than five percent to the natural fluorescence signal. The laser delivery and signal collection optics are shown in Fig. 2.

Several rapid (~ 10 s) scans were taken at each data point. The rapid scans prevented long lock-in time constants from artificially shifting the fluorescence spectra to lower frequencies which would falsely indicate lower velocities. These scans were then Chauvenat filtered and averaged.

Theory

Laser-Induced Fluorescence

The absorbing neutral xenon, Xe I, or singly ionized xenon, Xe II, will "see" the wavelength of the incoming laser photons shifted by the relative motion of the particle in the direction of the photon.

$$\nu = \nu_0 \left(\frac{v_i}{c} \right) \qquad (1)$$

The velocity components from the various laser beams are extracted by a straight forward geometrical regression.[10] The temperatures associated with each component are elliptically related assuming statistical independence.[10] The velocity distributions were calculated via Eqn. 1 assuming Gaussian profiles about the bulk velocity. The energy distributions were calculated directly from the velocity distributions:

$$E[V] = \frac{mv_i^2}{2e} \qquad (2)$$

Lineshape Models

A detailed lineshape model was used to determine the temperature and Doppler shifts of the fluorescence signals.[10] Only Gaussian broadening was considered since the magnetic fields, Stark broadening, and natural line widths

are negligibly small. However, because detailed spectral data were unavailable for the Xe I, Mo, and W transitions, a simpler model was employed.[13]

Neutral density filters were periodically placed in the laser beam path to check for saturation. There was no indication of saturation during 4-beam operation. However, during 1-beam interrogation of Mo, the fluorescence FWHM varied significantly. Saturation intensity can be approximated by[14]

$$I_{SAT} = \frac{hc}{2\sigma\sigma_i} A_{ji} , \qquad (3)$$

where the cross-section was approximated from tabulated spectral data.[15]

$$\sigma = A_{21} \frac{\lambda^2}{8\pi} g(\nu_0).$$

The power-broadened fluorescence lineshape takes the form[14]

$$\ell(\nu) = \frac{\gamma/2}{(\nu - \nu_0)^2 + (\gamma/2)^2 \left(1 + I/I_{SAT} \right)} \qquad (4)$$

The homogeneous relaxation rate, γ, is a combination of natural and collisional relaxation rates. As discussed below, these are assumed to be roughly of the same order of magnitude in this investigation: $\gamma \approx A_{ji}/2$. The power-broadened lineshape was convolved with a Gaussian lineshape,

$$g(\nu) = \frac{c}{\nu_0} \left(\frac{m}{2\pi kT} \right)^{1/2} \exp \left(-4ln(2) \frac{(\nu - \nu_0)^2}{\nu_D^2} \right) \qquad (5)$$

to fit the Mo data yielding a more accurate estimate of the temperature.

Erosion-rate Measurement

The natural population of the lower state of the pump transition may vary with cathode operating condition. In order to correlate LIF signal with the density of sputtered species, this variation must be accounted for. The most straight forward approximation is to assume local thermodynamic equilibrium (LTE) and,

3

given the temperature from the LIF data, calculate the relative natural populations:[16]

$$I(\lambda ,T) = \frac{2hc^2}{\lambda^5 \left[\exp\left(\frac{hc}{\lambda kT}\right) - 1\right]} \quad (6)$$

Assumption of LTE is valid if[17]

$$n_e n_j R_{CD} \gg 10 n_j \sum_{i,i<j} A_{ji} \quad (7)$$

where

$$R_{CD} = 1.58 \times 10^{-5} \frac{g_i}{g_j} \frac{f_{ij}\langle G \rangle}{E_{ij}T_e^{1/2}} n_e .$$

Because n_e is unknown and the spectral constants are poorly known, this relation only gives an indication of the suitability of assuming LTE. For a discharge voltage of 25 V, n_e on the order of $10^8 cm^{-3}$ is required. As n_e on centerline, just downstream of the exit of the DCA has been measured to be on the order of $10^{12} cm^{-3}$, LTE appears justified even 0.5 cm off centerline.[18]

Results

Erosion

A typical W LIF signal is shown in Fig. 4. The DCA data were taken 0.3 cm off centerline, 0.05 cm downstream of the un-keepered DCA operating at 12 A, 27 V. The W reference data were taken with the W target biased 100 V below cathode potential. The first order fit is shown with open markers. The fit indicated that the reference data had a temperature of 1000 K.

A typical Mo LIF signal is shown in Fig. 5. The Mo reference data were taken in the same Hamamatsu cell used to generate the Xe I and Xe II reference signals. The temperature indicated by the fit of the reference cell data, 800 K, is within 50 K of the Xe I and Xe II data taken at the same cell voltage and current.

Un-keepered

Figure 6 shows Mo and W LIF signals as a function of radial position as indicated by a picture of the exit plane of the un-keepered DCA. Note that the signals peak at roughly the same radial position (0.3 cm) and indicate erosion peaks near the transition from the cathode orifice plate (W) to the cathode tube (Mo). The resolution of the LIF technique (roughly 0.05 cm) did not allow a more detailed mapping. Mo data were only taken over half of the diameter.

Subsequent Mo data were taken at the 0.3 cm location because the Mo surface subject to impinging ions is limited to this region. W data were taken at roughly the same point for comparison.

Figure 7 shows the Mo LIF signal strength as a function of discharge current. Note that there is a noticeable increase in signal with current. Also shown in the figure is the signal corrected for temperature which tends to collapse the data to a monotonically increasing function of J_D. There is a non-negligible signal at $J_D =6.0$ A. Data taken at $V_D = 27$ V show that the Mo LIF signal also increases with discharge voltage.

The Mo temperature was roughly constant at 2000 K implying that variations in the temperature were within the 20 percent uncertainty in temperature measurement. Xenon neutral temperatures varied between 2000 and 2500 K when corrected for saturation effects. Typical Xe I data ($J_D = 13.1$ A) are given in Fig. 8.

Figure 9 shows W LIF data as a function of discharge current and discharge voltage. The signal is roughly constant with discharge current below 12 A, above which it increases significantly. The W temperatures varied between 2000 and 3000 K. However, the data were very noisy and introduced an uncertainty of roughly 30 percent.

Figure 10 shows Mo and W orifice plate erosion rates as a function of operating condition. The conversion from LIF signal to erosion rate is based on the assumption that similar operating conditions yield similar erosion rates. Thus, the 12 A, 27 V erosion rate was set to the value measured in the 2000 hr wear-test and the other data were scaled accordingly in order to show the dependence of the erosion rate on the operating condition. Note that the Mo data show a greater dependence on operating condition. The 12 A, 27 V condition had a significantly higher signal and temperature than other conditions. Correcting for saturation and temperature yielded a signal consistent with those at other operating conditions. Assigning the nominal wear-test value to this anomalous point may introduces additional uncertainty in the predicted Mo erosion rates at other conditions, but the trends in those conditions should be accurate.

Keepered

Figure 11 shows the variation in Mo LIF signal across the face of the DCA keeper. The picture of the keeper provides a reference for radial position. The data were taken 0.05 cm downstream of the keeper orifice plate. The signal maximum is at roughly 0.5 cm. Limits in optical access prevented measurement beyond 1 cm. Subsequent Mo data were taken at the 0.5 cm point. No W data were collected for keepered operation.

Figure 12 shows Mo LIF signal and temperature-corrected data as a function of discharge current for $V_D = 25$ V and 27 V. A strong dependence on current is evident, and the signal is non-negligible at $J_D = 8.2$ A Unlike the un-keepered data, temperature corrections appear to remove the dependence on discharge voltage over this small range.

Pure Gaussian fitting (Eqn. 5) of the keepered Mo signals yielded temperatures between 8000 and 11000 K. Corrected for saturation, the temperatures varied between 2000 and 3000 K. Neutral xenon data yielded temperatures varying between 2500 and 3500 K. Xe I data were collected for $J_D = 8.2$ and 13.1 A (25 V).

Figure 13 shows the keeper erosion-rate as a function of operating condition assuming the 13 A, 25 V case produces a rate similar to that measured in the 8000 hr life-test. Note that, as in the un-keepered Mo data, there is a noticeable dependence on J_D and that the curve is fairly smooth.

Ion velocities

Four-beam LIF yielded Xe II velocities and temperatures in the region downstream of the DCA. A typical set of data is given in Fig. 14. These data were taken on centerline, 0.5 cm downstream of the un-keepered DCA at 12 A, 27 V. Note the close proximity of the 4 curves which illustrate the sensitivity to the size and resolution of the beam angles. The de-convolution algorithm was used to calculate the velocities and the temperatures were estimated by fitting the resulting velocity profiles with Gaussian distributions (Eqn. 5).

Un-keepered ion velocities

Figure 15 compares mean axial centerline velocities for various un-keepered DCA/FMT operating conditions. An error of roughly 20 percent reflects both the uncertainty in the measurement of axial angles and and in the location of the reference cell peaks. While the magnitudes of the velocities depend on the specific operating condition, the data do indicate several trends. There is a region of low-velocity/back-flowing ions just downstream of the orifice. The velocities then increase to a peak roughly 1 cm downstream and then remain at that level. Higher J_D leads to higher velocities downstream. Higher V_D yields lower velocities and back-flowing ions at the cathode exit plane.

Figure 16 maps the ion velocities downstream of the DCA for the condition corresponding to that of the 2000 hr wear-test, i.e. 12 A, 27 V. Note the back-flowing ions near the 0.3 cm radial position and the high off-axis velocities along the face of the DCA. The region of transition from low to high velocity appears as a quiescent region between 0.3 and 0.6 cm downstream.

Energy distributions along the face of the cathode for this same condition are given in Figure 17. Note that magnitudes of back-flowing ion energies peak near the location of maximum erosion, 0.4 to 0.6 cm. In this region, a significant fraction of the ions were flowing back towards the cathode. These data agree with previous investigations at higher discharge voltages.[8,13]

Keepered

Figure 18 compares mean axial centerline velocities for various keepered DCA/FMT operating conditions. As in Fig. 15, the data largely follow a trend, though significantly different than that in Fig. 15. The velocities start small and or negative but, then, increase quickly to a high velocity (>3000 m/s) within 0.2 cm. The velocities then decrease significantly (except for the 12 A, 32 V data which remain at a low velocity, 100 m/s). Most, then increase again to values comparable to those 1.5 cm downstream of the un-keepered DCA. A notable exception to this trend is the 13 A, 25 V data which experiences smaller fluctuations.

Figure 19 maps the ion velocities downstream of the DCA for the 13 A, 25 V condition (which again corresponds to that of the 8000 hr life-test). Note the back-flowing ions near the 0.6 cm radial position and the high off-axis velocities along the centerline. The ions are back-flowing both axially and radially. There is a region of low velocity between 0.1 and 0.2 cm downstream of the keeper exit plane.

Energy distributions along the face of the keeper are given in Figure 20 for this case. Note that magnitudes of back-flowing ion energies

peak near the location of maximum erosion, and that at the 0.6 cm location a significant fraction of the ions are flowing back towards the cathode.

Ion densities

The magnitude of the LIF signal provided a rough estimate of the relative Xe II densities downstream of the DCA. The un-keepered data show an extended region of high density whereas the keepered data show a more localized peak just downstream of the keeper. The LIF signal strength significantly decreased radially outwards along the face of the cathode.

The ion density at the exit of the DCA has been measured to be on the order of 10^{12} cm^{-3} for 6 A, 18 V HCA operation.[18] Conservatively estimating the density to be similar for 12 to 13 A operation, the density at 0.3 cm in the 12.1 A, 26.8 V case would be on the order of 10^{10} cm^{-3}. At 0.6 cm for the 13.1 A case, $n_e = n_I$ would be on the order of 10^{12} cm^{-3}. At 0.6 cm off-axis near the orifice, the densities are one to two orders of magnitude lower.

Discussion

Erosion

The location of peak Mo and W LIF signal is in very good agreement with the observed regions of erosion. Because no absolute erosion rates were made, no comparison can be made between the W and Mo erosion rates.

The un-keepered Mo LIF signal in Figs. 7 and 10 shows an anomalous peak at the 12 A, 27 V condition. Possible explanations of this include the formation of a large potential–hill downstream of the orifice resulting from the relatively low cathode flow rate. However, it is more likely a result of the temperature/saturation correction scheme. As seen especially in the keepered Mo data, this scheme typically significantly reduces the apparent effect of discharge voltage present in the raw data. A more detailed model and data reduction routine is under development.

The throttling of NSTAR and post-NSTAR 30 cm ion thrusters is nominally done at constant discharge voltage.[9] Therefore, the trends evident in the 25 V data are still of value despite the significant uncertainty in absolute value. Note that both keepered and un-keepered data show a gradual rise in predicted erosion rate with discharge current (Figs 10 and 13). Modest changes in J_D below 12 A will not significantly reduce the erosion. However, increasing J_D

above 12 A may significantly increase it unless the discharge voltage is decreased.

These trends indicate that the reduced erosion observed in the 1000 hr wear-test and 8000 life-test resulted in part from counter-acting contributions of a decrease in discharge voltage and an increase in discharge current. However, since the erosion rates and ion distributions varied only slightly with the variation of these parameters, this investigation would suggest that, alone, these counter-acting contributions would only slightly decrease the overall erosion.

Ion velocities

The keeper electrode significantly modified the structure of the plasma downstream of the DCA. In particular, the ions appeared to be created in a more collimated region in the keepered cases . This appeared to affect the size and location of a potential-hill, influencing ion paths near the DCA surfaces.

The presence of a potential-hill is strongly suggested by the decrease in axial velocities in the keepered case (Fig. 18). Note that in both keepered and un-keepered configurations the DCA runs near plume-mode. In such a mode, the region of ionization required to draw electrons out of the cathode extends significantly downstream of the cathode/keeper orifice.[5] Such operation is conducive to the formation of a potential-hill.[7] The extended region of increasing ion velocities downstream of the un-keepered DCA (Fig. 15) also suggests a potential-hill.[8]

The proximity of the potential hill to the DCA exit plane appears proportional to the back-flowing component of the ions which are rapidly moving off-axis from the region of ionization near the DCA exit in all cases. The extended region of acceleration downstream of the un-keepered DCA indicates that the hill is near the exit, hence no significant deceleration further downstream. Conversely, the rapid increase in ion velocity followed by a region of deceleration indicates that a potential-hill exits on the order of 1 cm from the keepered DCA. Thus, the back-flowing components of the radially escaping ions would be expected to be greater in the un-keepered case. That is what is observed.

Figure 19 shows that most ions impacting the DCA surface in the keepered configuration are actually moving towards the cathode centerline. This suggests that a different mechanism of ion acceleration is in part responsible for the erosion. Note that there are

ions impacting the surface with axial and radial back-flowing velocity components near the limits of the LIF interrogation in both keepered and un-keepered configurations (Figs. 16 and 19). Perhaps the proximity of the potential-hill in the un-keepered case tends to mask the presence of these ions closer to the centerline.

The angle of incidence of most of the ions striking the surface in the velocity maps is on the order of 45 degrees. This is approaching the optimal angle for sputtering of roughly 55 degrees. [8] Coupled with the potential drop across the sheath on the cathode, the Xe II ions would then have sufficient energy to erode the surface. However, it is unclear whether the density fo the ion is sufficient to generate the measured erosion rates. Xenon III ions should follow the same paths as Xe II ions and may result in the majority of the erosion [8]

Conclusions

The use of LIF to measure real-time internal erosion rates has been demonstrated. W, Mo, Xe I, and Xe II species were interrogated to provide a clear picture of the discharge cathode erosion process. Spatial variations in LIF signal strengths agree with measured erosion patterns.

The Mo, and to a lesser extent W, LIF signals were proportional to the discharge current and voltage. The data indicate that operating at lower currents and lower voltages will reduce erosion. However, reduction of J_D below 12 A appears to have only a marginal effect .

The erosion and ion velocity data support a general explanation of the DCA erosion process: erosion is caused by back-flowing ions created just downstream of the DCA exit plane. The presence of the keeper electrode appears to change the density distribution but has only a marginal affect on the velocity distribution. Significant radial velocities and back-flowing ions were observed with and without the keeper.

One source of the back-flowing ions appears to be a potential hill located within 1 cm of the DCA exit plane. The magnitude of the hill is proportional to discharge voltage and also to discharge current. Ions move radially from their region of creation at high velocities. The more significant the potential-hill, the greater the back-flowing component of these ions.

The presence of back-flowing ions with radial velocities towards the centerline indicate the presence of an additional mechanism. As the density of ions increases near the edges of the cathode or keeper, a greater fraction of these ions is drawn back towards the lower potential of the DCA surface. This mechanism appears to be secondary as evidenced by the significantly smaller erosion rates measured on the keeper electrode.

Future Work

Since the LIF data were time averaged over tens of seconds, erosion induced by fluctuations in the plasma would also have been indistinguishable from that caused by steady-state ion impingement. Equally, the ion velocities would be time-averaged and may or may not include contributions from these effects. While it is know that fluctuations in the cathode voltage are present,[8] the resolution of ion velocities and erosion measurements on time scales of μs was beyond the scope of this investigation.

The combination of small angles between interrogating beams and of fluctuations in the reference cell datum resulted in significant uncertainty in the ion velocity measurements. While the reference cell was stabilized, the angles could not be increased without significantly modifying the FMT. While technically possible, such modifications (e.g. providing optical access into the discharge chamber from just upstream of the ion grids) were beyond the scope of this investigation. However, doubling or tripling the angles of interrogation would increase the velocity resolution significantly and would provide a more rigorous quantification of the influence of the potential-hill.

A calibrated ion source could provide a real-time calibration of the erosion species LIF. This would provide a real-time absolute erosion-rate capability. Detailed spectral line modeling would provide a much more accurate measurement of the temperature of these species which would yield greater accuracy in the conversion of LIF signal to erosion rate measurement. Also, a multiplex LIF tool with greater axial angles of interrogation would significantly increase the accuracy of the axial ion velocity measurements. This would entail modification of the optical access to the FMT. All of these are left to future investigations.

References

[1] Patterson, M. J., et al, "2.3 kW Ion Thruster Wear Test," AIAA-95-2516, 31st Joint Propulsion Conference (July, 1995).

[2] Polk, J. E., et al, "A 1000-Hour Wear Test of the NASA NSTAR Ion Thruster," AIAA-96-2717, 32nd Joint Propulsion Conference (July, 1996).

[3] Polk, J. E., "An Overview of the Results from an 8200 Hour Wear Test of the NSTAR Ion Thruster," AIAA-99-2446, 35th Joint Propulsion Conference (June, 1999).

[4] Brophy, J. R., et al, "The Ion Propulsion System on NASA's Space Technology 4/Champollion Comet Rendezvous Mission," AIAA-99-2856, 35th Joint Propulsion Conference (June, 1999).

[5] Domonkos, M. T., "Evaluation of Low-Current Orificed Hollow Cathodes," Ph.D. Thesis, The University of Michigan, October, 1999, pp 153-157.

[6] Katz, I., and Patterson, M. J., "Optimizing Plasma Contactors for Electrodynamic Tether Missions," Presented at Tether Technology Interchange, September 9, 1997, Huntsville, AL.

[7] Kameyama, I., and P. J. Wilbur, "Potential-Hill Model of High-Energy Ion Production Near High-Current Hollow Cathodes," ISTS-98-Aa2-17, 21st International Symposium on Space Technology and Science, (May, 1998).

[8] Williams, G. J., et al, "Characterization of the FMT-2 Discharge Cathode Plume," IEPC-99-104, 26the International Electric Propulsion Conference (October, 1999).

[9] Rawlin, V. K., et al, "NSTAR Flight Thruster Qualification Testing," AIAA-98-3936, 34the Joint Propulsion Conference (July, 1998).

[10] Williams, G. J., et al, "Laser Induced Fluorescence Measurement of the Ion Velocity Distribution in the Plume of a Hall Thruster," AIAA-99-2424, 35th Joint Propulsion conference (June, 1999).

[11] Striganov, A. R., and N. S. Sventitskii, Tables of Spectral Lines of Neutral and Ionized Atoms, Plenum, New York, 19668, pp 571-607.

[12] Corliss, C. H., and W. R. Bozman, Experimental Transition Probabilities for Spectral Lines of Seventy Elements, National Bureau of Standards Monograph 53, 1962, pp195-219 and 499-519.

[13] Williams, G. J., et al, "Laser Induced Fluorescence Characterization of Ions Emitted from Hollow Cathodes," AIAA-99-2862 (June, 1999).

[14] Miles, R., "Lasers and Optics," Course notes, Princeton University, 1995.

[15] Verdeyn, J. T., Laser Electronics, 3rd ed., Prentice-Hall, 1995, p 216.

[16] Incropera, F. P., and D. P. DeWitt, Fundamentals of Heat and Mass Transfer, 3rd ed., John Wiley and Sons, 1990, pp 710-711.

[17] Rock, B. A., "Development of an Optical Emission Model for the Determination of Sputtering Rates in Ion Thruster Propulsion Systems," Ph.D. Dissertation, Arizona State University, 1984, pp 43-59.

[18] Williams, G. J., et al, "Near-field Investigation of Ions Emitted from a Hollow Cathode Assembly Operating at Low-Power," AIAA-98-3658, 34the Joint Propulsion Conference (July, 1998).

Table 1: DCA/FMT Operating Conditions

Designation	J_D (A)	V_D (V)	P (kW)	m_C (sccm)	m_M (sccm)	TH
4 A	6.05	25.4	1.0	2.50	8.3	4
8 A	8.24	25.4	1.5	2.50	14.4	8
10 A	10.2	25.4	2.0	2.60	19.0	11
12 A, 25 V	12.1	25.1	2.3	2.90	24.0	-
12 A, 27 V	12.1	26.8	2.3	3.00	23.0	2000 hr wear-test
12 A, 32 V	12.1	32.2	2.3	2.65	21.0	-
12.5 A	12.6	25.4	2.2	3.10	24.0	-
13 A, 25 V	13.1	25.1	2.3	3.70	24.0	15
13 A, 27 V	13.1	26.8	2.4	2.90	24.0	-
13.5 A	13.6	25.1	2.3	3.20	24.0	-

Where: J_D = discharge current,
V_D = discharge voltage,
P = Thruster power
m_C = discharge cathode flow rate
m_M = main flow rate
TH = NSTAR/DS1 throttling point

Table 2: LIF Interrogation angles.

	(deg)	(deg)	(deg)
Un-keepered data	10.51±0.40	7.697±0.42	4.480±0.42
Keepered data	10.57±0.41	7.737±0.47	4.232±0.23

Table 3: LIF Transitions[11,12]

Species	Laser (nm)	Term Symbols {Energy levels (eV)}	Fluorescence (nm)	Term Symbols [Energy levels (eV)]	I_{SAT} (mW/cm^2)
Xe I	582.389	6s'[1/2]°—5f[1 1/2] {9.45—11.57}	617.967	6s'[1/2]°—5f[1 1/2] {9.57—11.57}	100
Xe II	605.115	5d^{4}D—6p^{4}P° {11.83—13.89}	529.222	6s^{4}P—6p^{4}P° {11.54—13.89}	30
Mo	603.066	{1.06—2.49}	550.649	{0.93—2.49}	10
W	429.461	{0.25—2.26}	426.939	{0.25—2.27}	50

Heater eroded until flush with
orifice plate

Cathode tube (Mo) eroded and
Electron-beam weld now flush
(symmetric about centerline)

Edge of orifice place (W) beveled
(symmetric about the centerline)
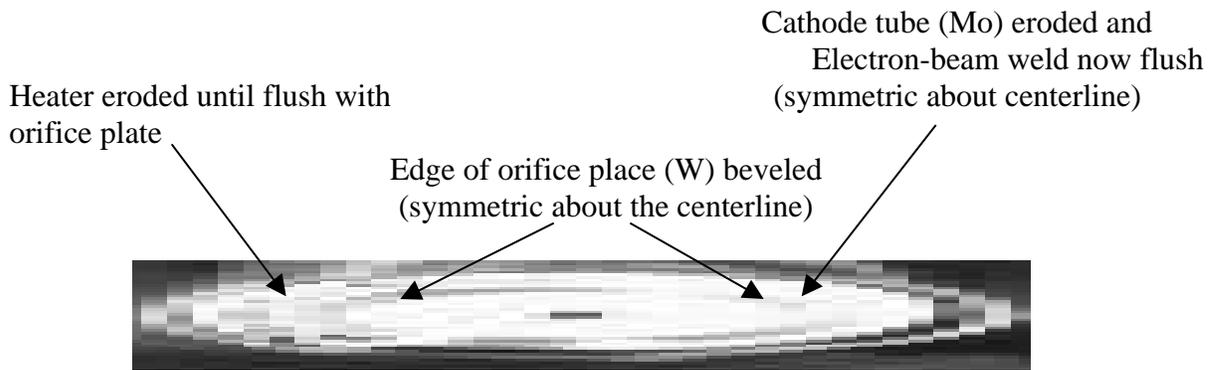
a. Photograph and sketch indicating un-keepered DCA erosion after 1000 hrs of the 2000 hr wear-test.

Downstream Face

Original Shape

Outer Edge

Deposits on Upstream Edge of Orifice

1.0 mm

Keeper Orifice
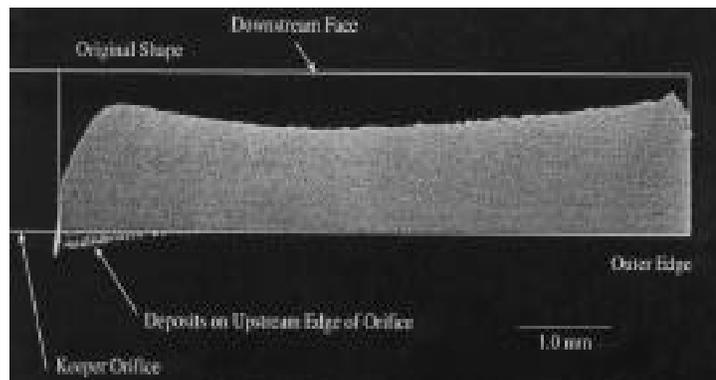
b. Photograph of the DCA keeper after the 8000 hr life-test.[3]

Figure.1 DCA erosion patterns.
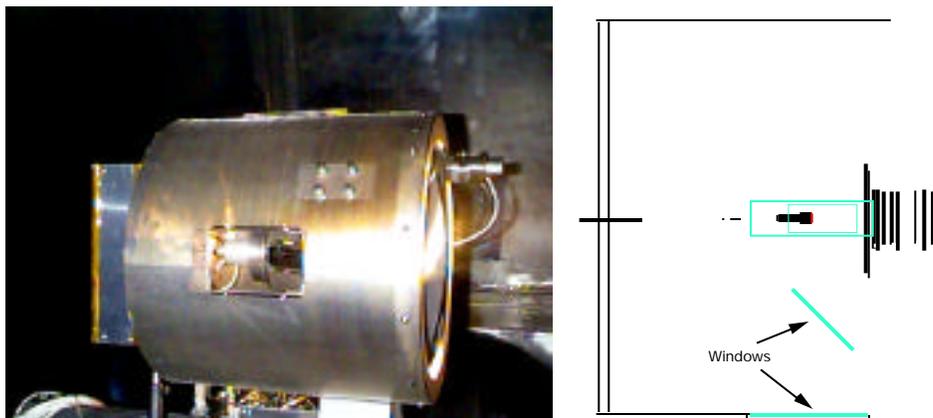
Windows

Figure 2 Photograph and schematic of the FMT 30 cm ion thruster. Note the location of the windows on the discharge chamber wall and the ground screen.
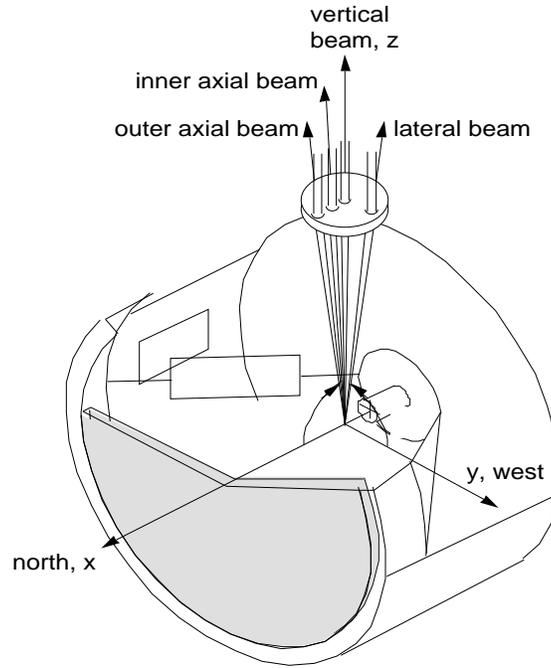
Figure 3 Schematic of laser beam delivery. Note the location of the beams on the lens.
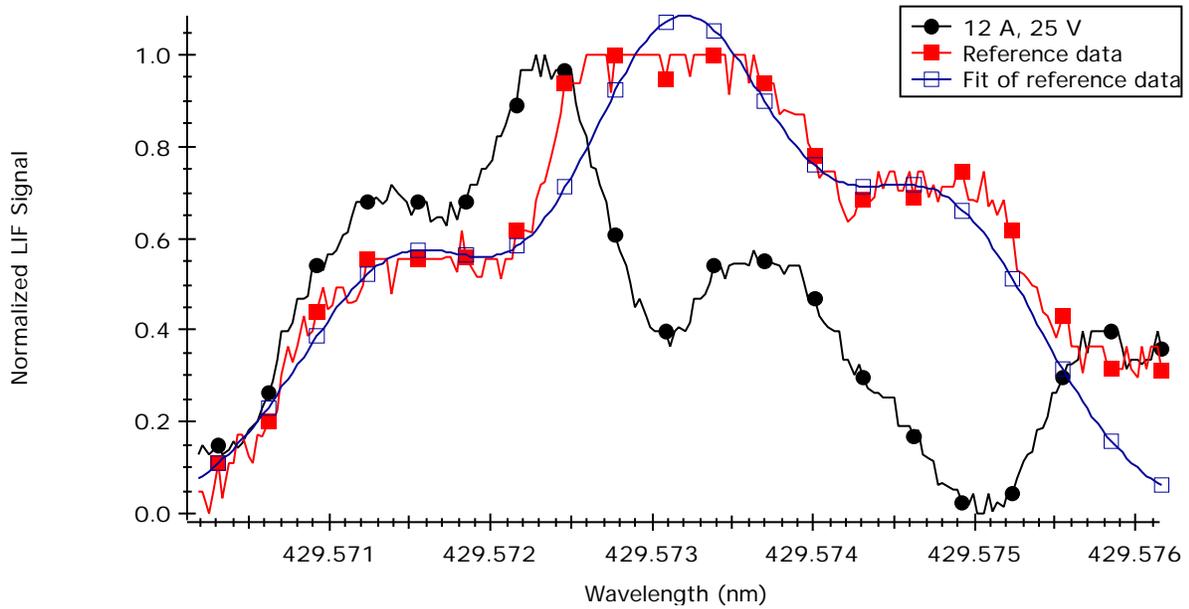
Figure 4 Typical W LIF data. Note that the slight offset of the data taken downstream of the DCA indicates an axial velocity on the order of 1000 m/s.
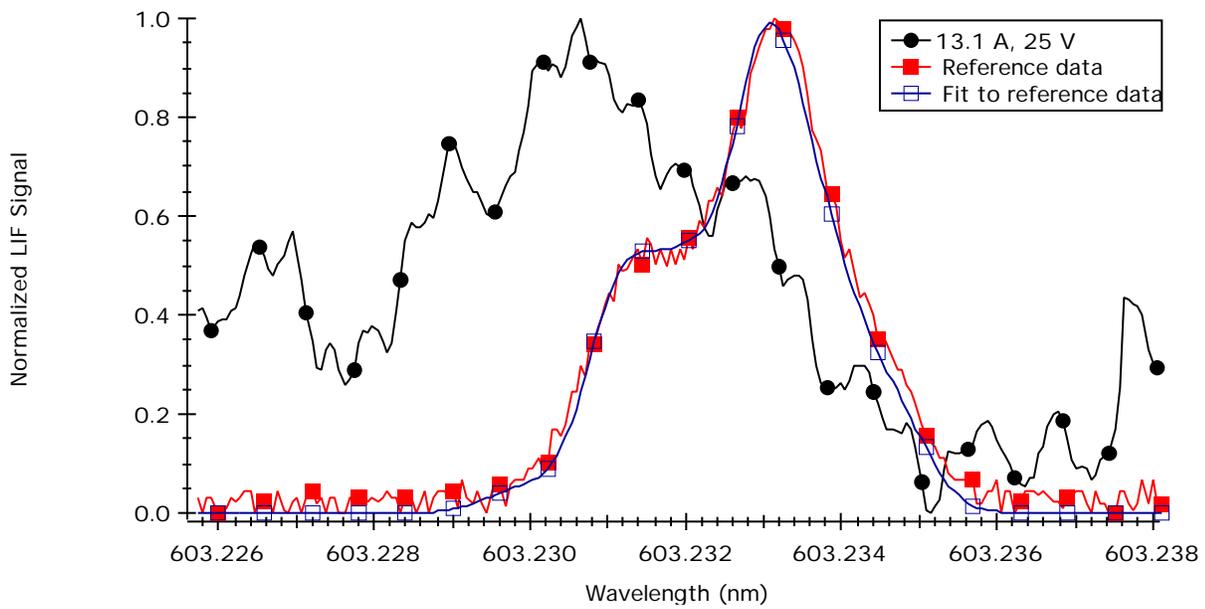
Figure 5 Typical Mo LIF data. The offset in the data corresponds to a velocity of roughly 500 m/s.
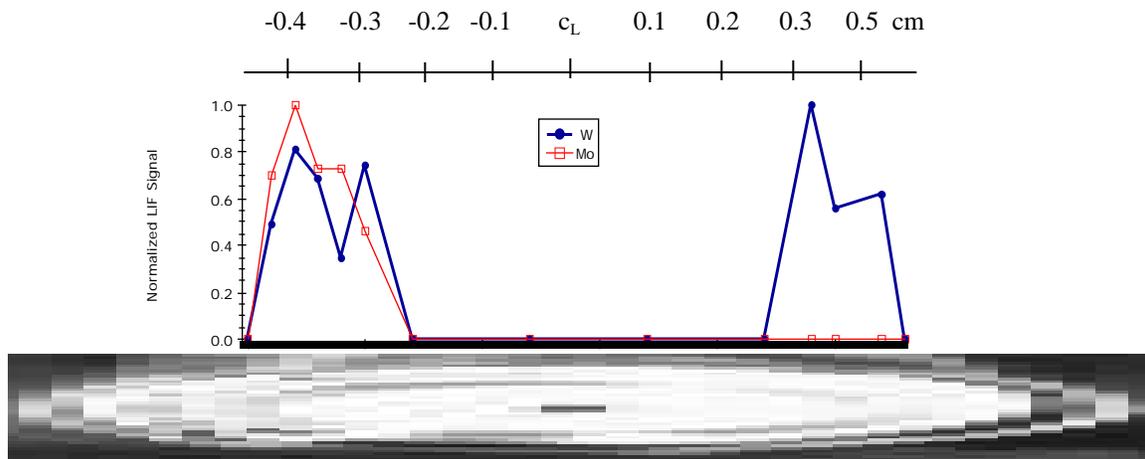
Figure 6 Radial distribution of Mo and W LIF signals which have been self-normalized. Note that no Mo data were taken right of centerline. Data shown are for 12 A, 27 V.
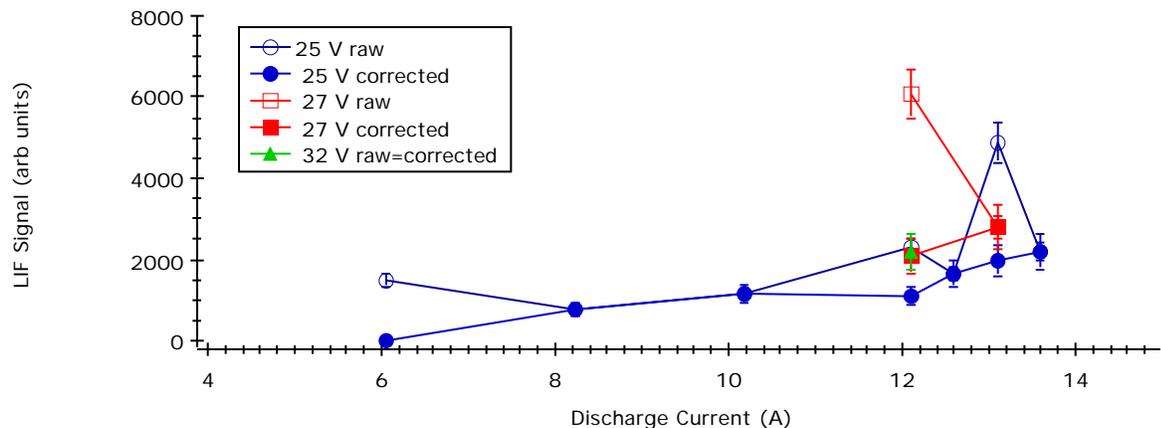
Figure 7 Mo LIF signal strength as a function of discharge current for 25, 27 and 32 V operation. Solid data markers indicate consideration of the temperature as indicated by the LIF scans: 2000 K was used as a reference for LTE scaling.
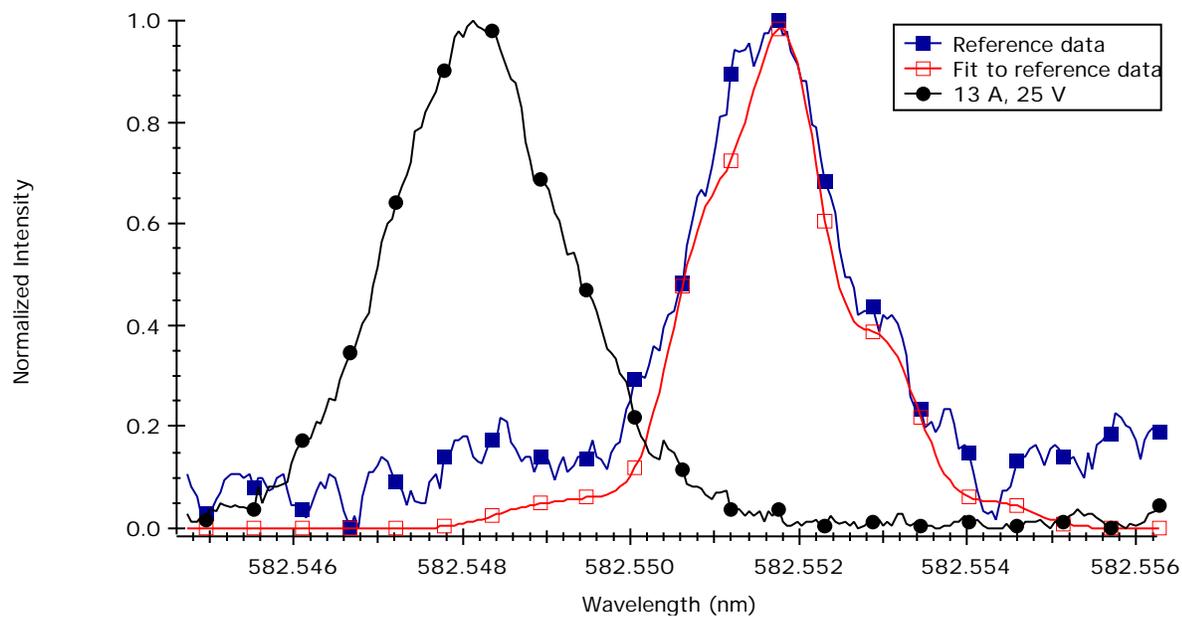
Figure 8 Typical Xe I LIF data. The offset corresponds to a velocity of roughly 1500 m/s.
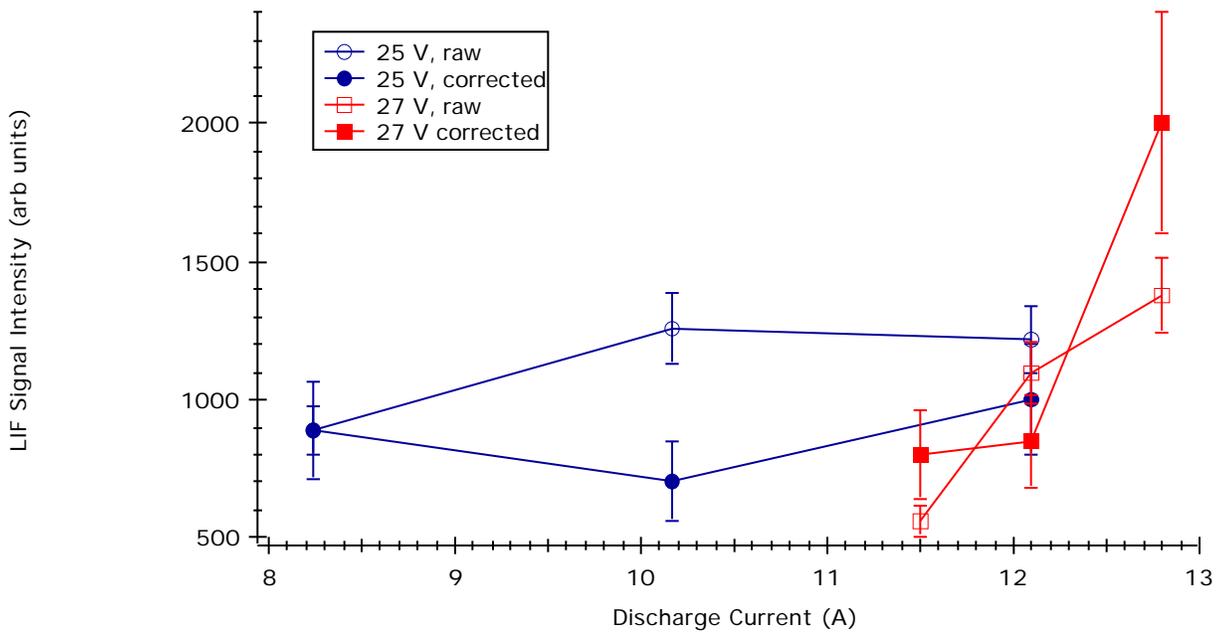
Figure 9 W LIF signal as a function of discharge current for V_D = 25 and 27 V. 3000 K was used as a reference for LTE scaling..
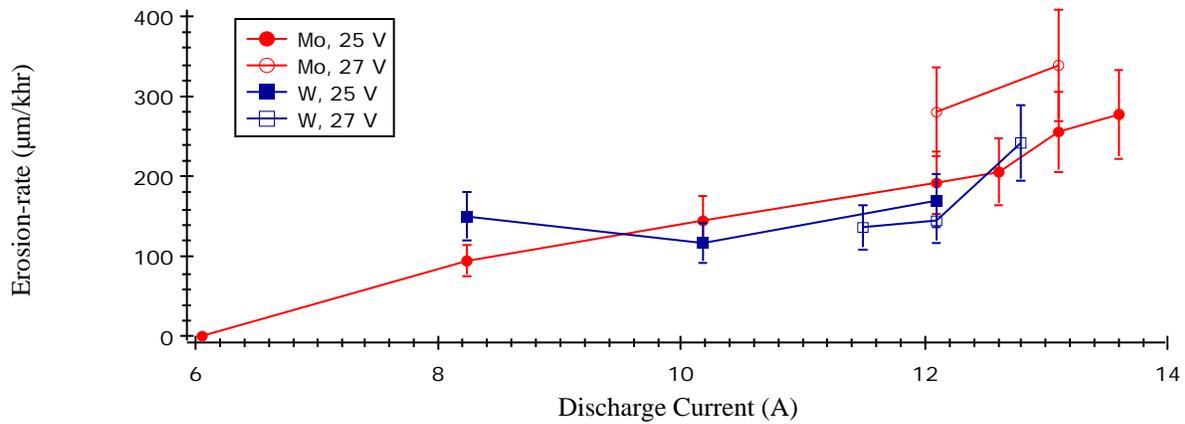
Figure 10 Erosion-rates predicted for un-keepered operation

10
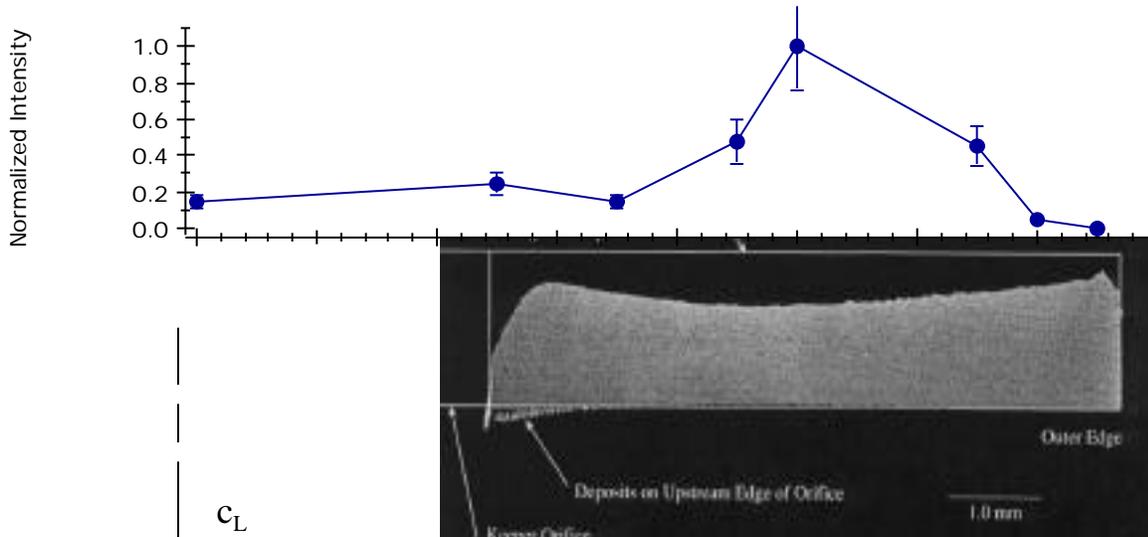
Figure 11 Mo LIF across the face of the keeper electrode for 13 A, 25 V. Note that the LIF signal corresponds to the erosion pattern.
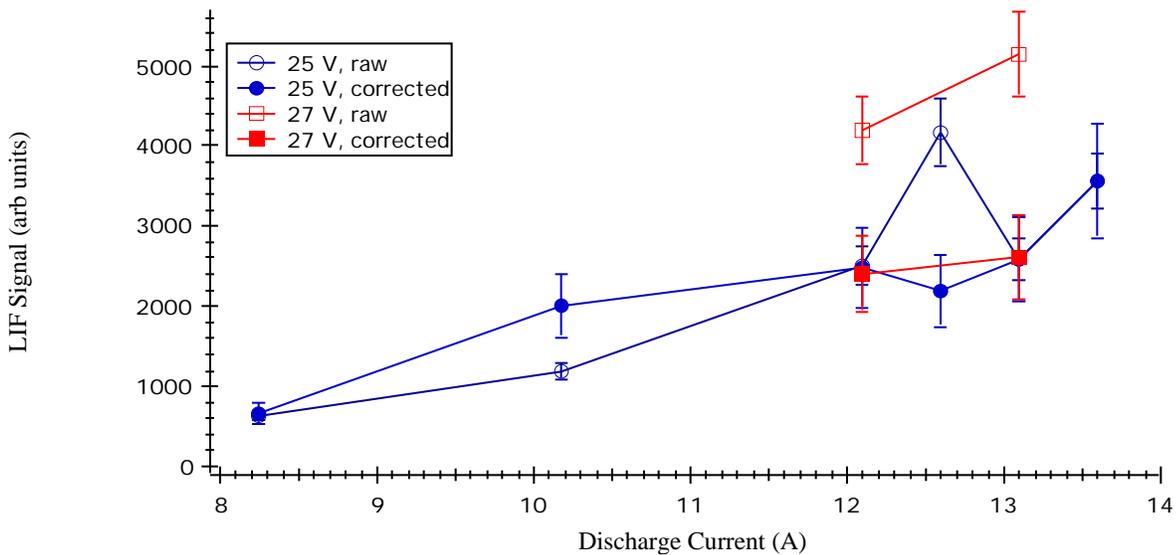
Figure 12 Mo LIF signal strength as a function of discharge current for V_D = 25 V and 27 V. The corrected values reflect the changes in temperature as measured by LIF: 3000 K was used as a reference for LTE scaling.
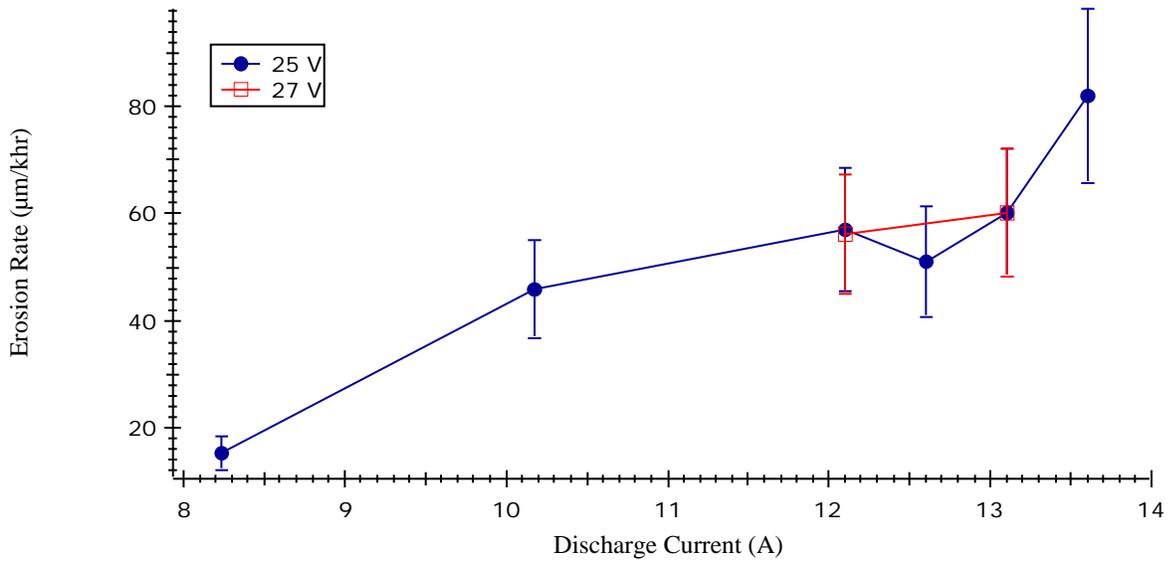
Figure 13 DCA keeper erosion rate estimates as a function of discharge current.
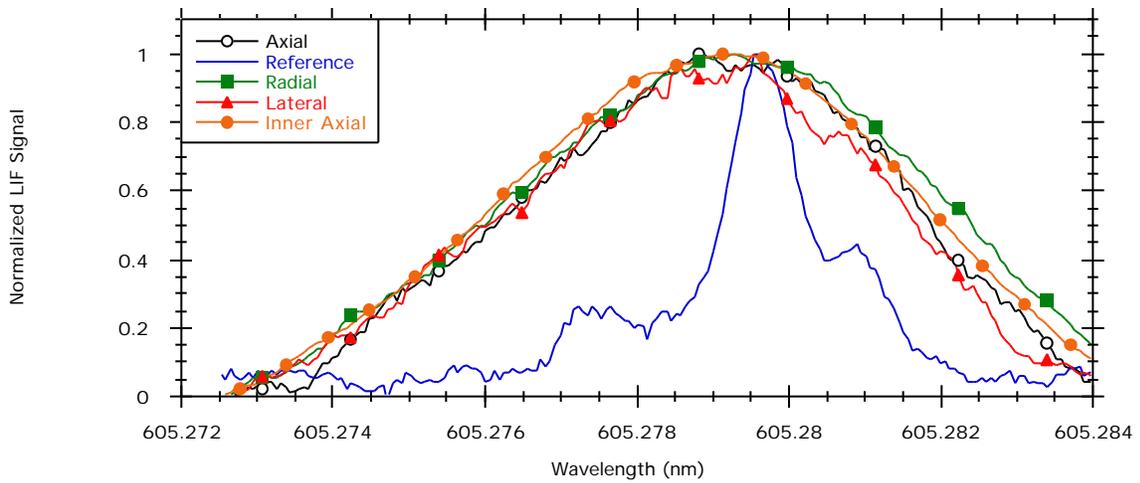
Figure 14 Typical Xe II LIF data. Data shown were taken on centerline, 0.5 cm downstream of the un-keepered DCA operating at 12 A, 27 V.
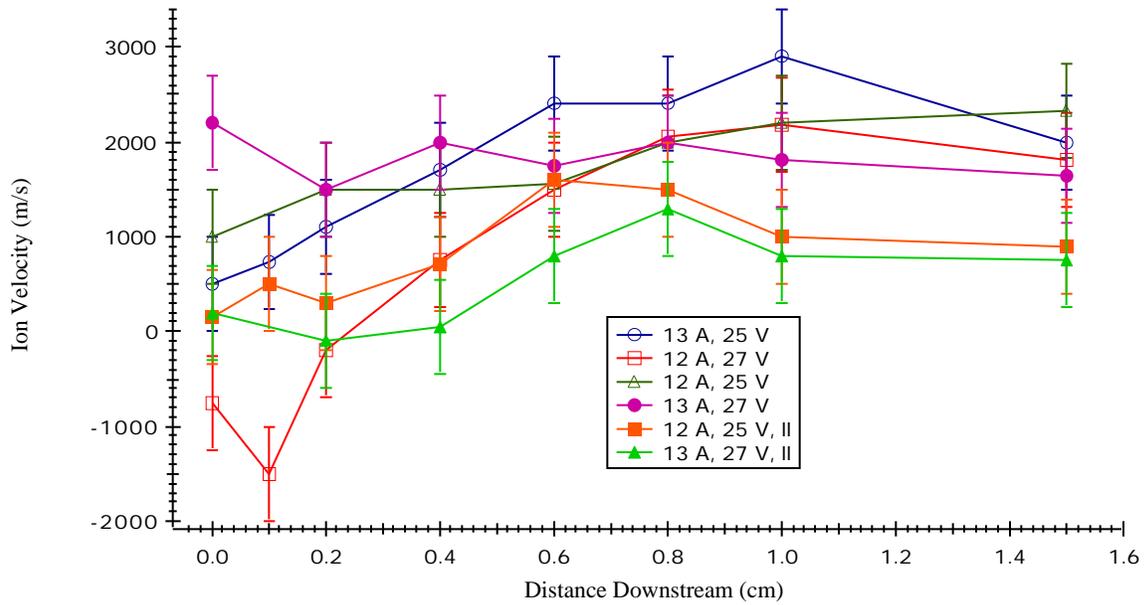
Figure 15 Centerline axial Xe II velocities downstream of the un-keepered DCA.
Note, 1eV = 1200 m/s.
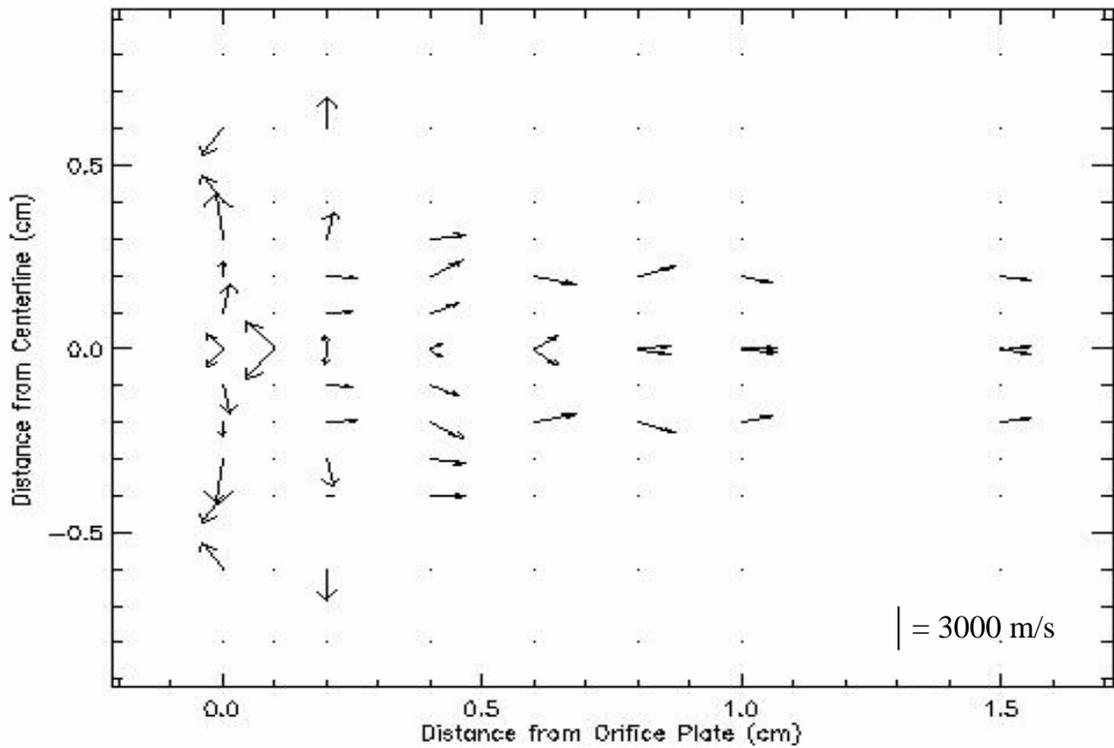
Figure 16 Xe II velocity map for 12 A, 27 V operation. Note the regions of back-flowing
ions along the cathode face (x=0) and the region of small velocities along the centerline
between 0.3 and 0.6 cm downstream.
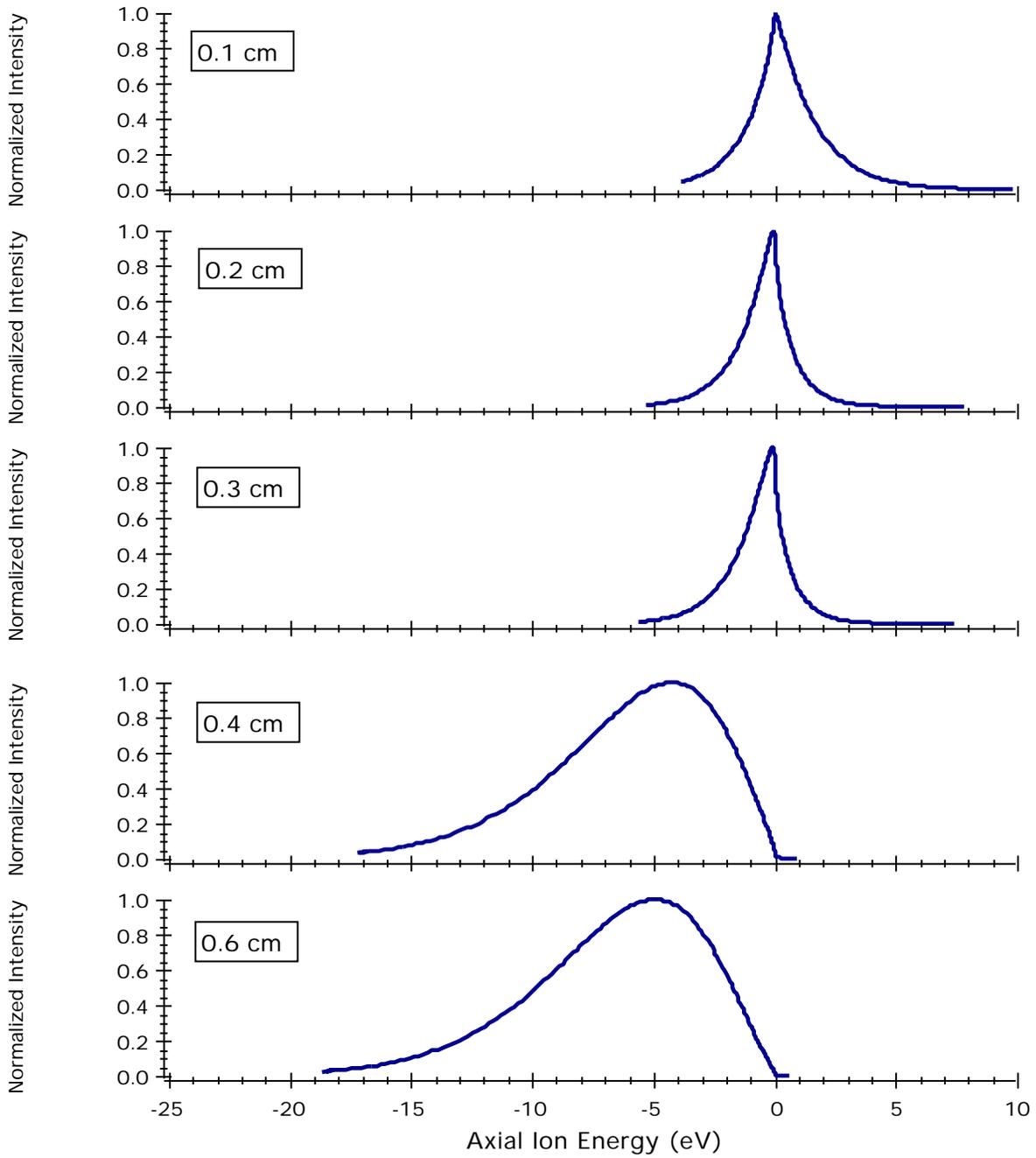
Figure 17 Normalized axial Xe II energy distributions as a function of radial distribution along the face of the un-keepered DCA for 12 A, 27 V operation.
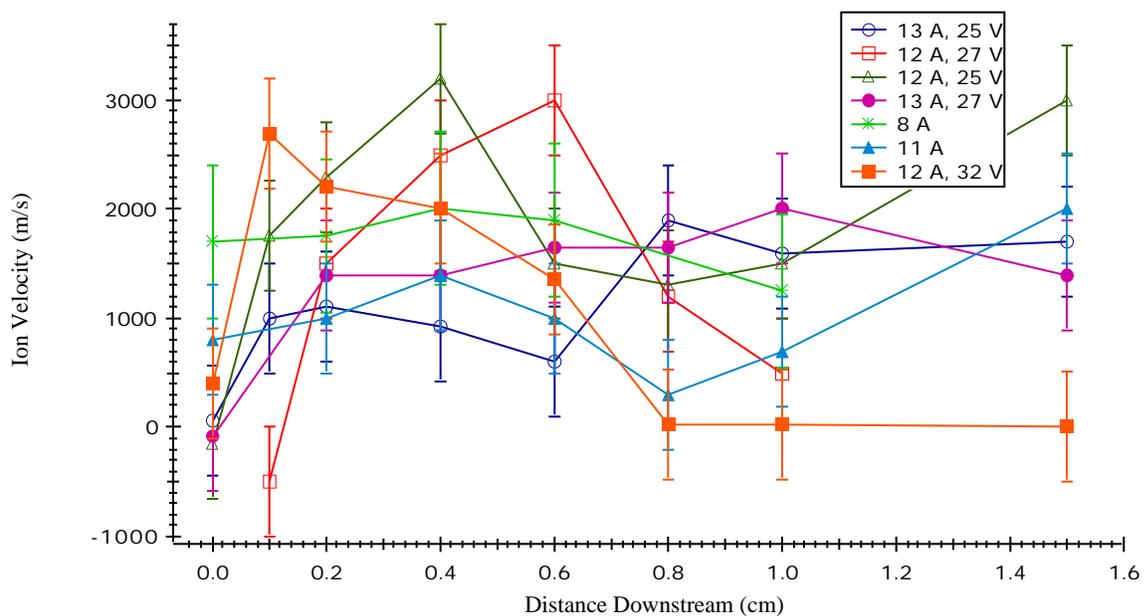
Figure 18 Centerline axial Xe II velocities downstream of the keepered DCA.
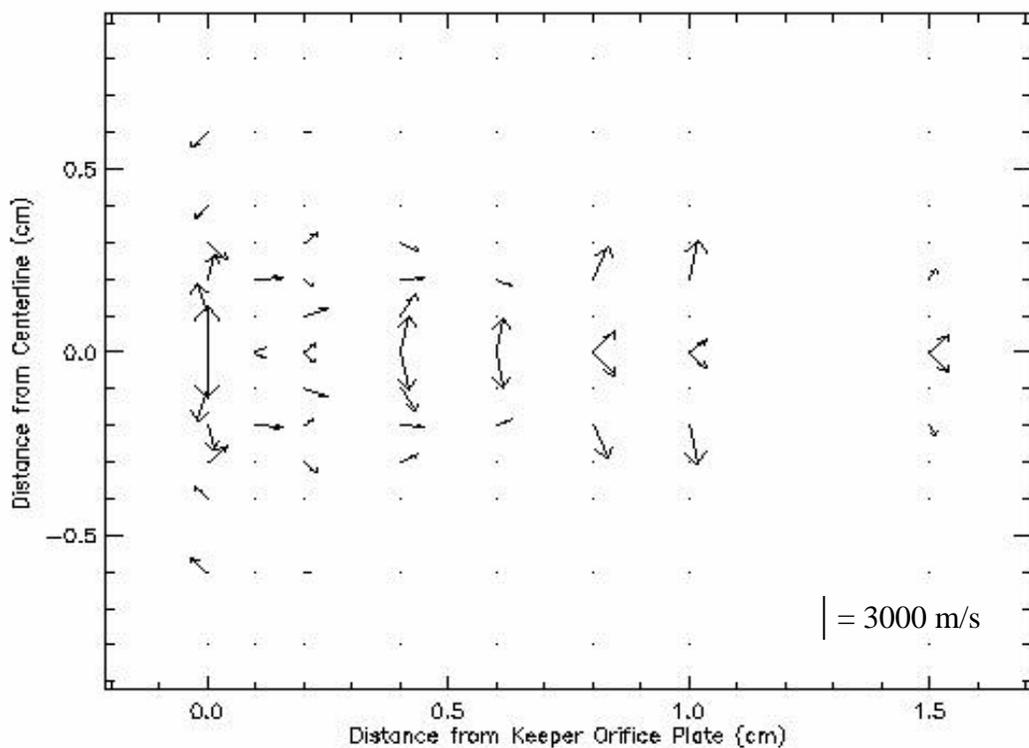
Figure 19 Xe II velocity map for 13 A, 25 V operation. Note the regions of back-flowing ions along the cathode face (x=0) and the region of small velocities along the centerline between 0.3 and 0.6 cm downstream.

10
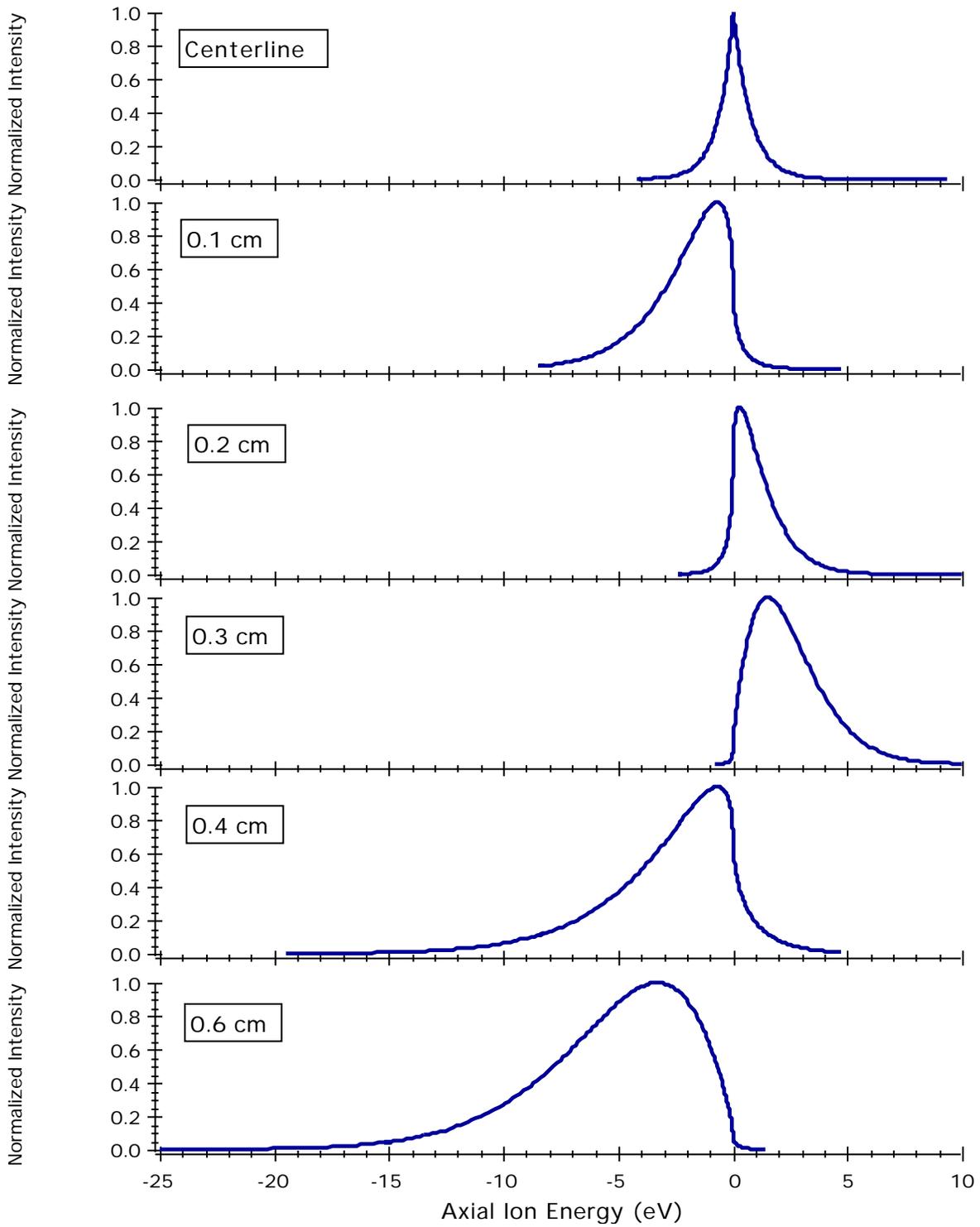
Figure 20 Energy distributions across the keeper face. Note the significant energies 0.4 and 0.6 cm downstream (roughly in the center of the keeper).
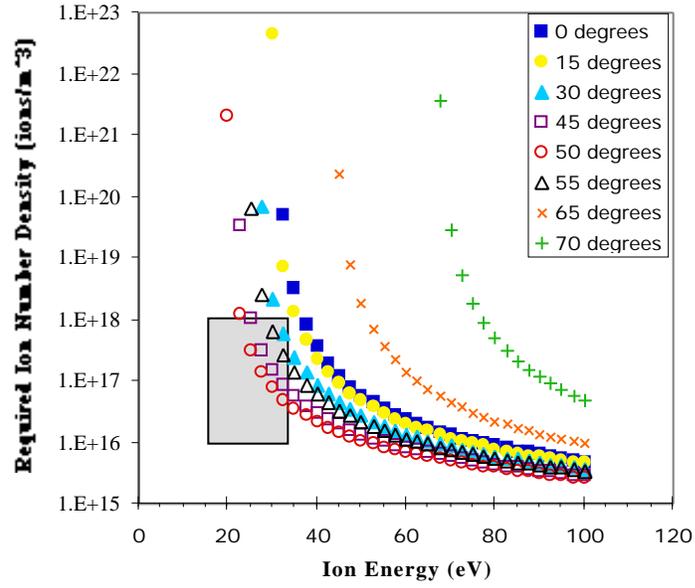
Figure 21 Number densities required to produce the erosion observed in the 2000 hr wear-test.